PHYSICAL REVIEW APPLIED **5**, 034008 (2016)

High-Resolution ac Measurements of the Hall Effect in Organic Field-Effect Transistors

Y. Chen,[1,*] H. T. Yi,[1] and V. Podzorov[1,2,†]
[1] *Department of Physics, Rutgers University, Piscataway, New Jersey 08854, USA*
[2] *Institute for Advanced Materials and Devices for Nanotechnology (IAMDN), Rutgers University, Piscataway, New Jersey 08854, USA*

(Received 16 December 2015; revised manuscript received 20 February 2016; published 17 March 2016)

We describe a high resolving power technique for Hall-effect measurements, efficient in determining Hall mobility and carrier density in organic field-effect transistors and other low-mobility systems. We utilize a small low-frequency ac magnetic field ($B_{\mathrm{rms}} < 0.25$ T) and a phase-sensitive (lock-in) detection of Hall voltage, with the necessary corrections for Faraday induction. This method significantly enhances the signal-to-noise ratio and eliminates the necessity of using high magnetic fields in Hall-effect studies. With the help of this method, we are able to obtain the Hall mobility and carrier density in organic transistors with a mobility as low as $\mu \sim 0.3\ \mathrm{cm^2\,V^{-1}\,s^{-1}}$ by using a compact desktop apparatus and low magnetic fields. We find a good agreement between Hall-effect and electric-field-effect measurements, indicating that, contrary to the common belief, certain organic semiconductors with mobilities below $1\ \mathrm{cm^2\,V^{-1}\,s^{-1}}$ can still exhibit a fully developed, band-semiconductor–like Hall effect, with the Hall mobility and carrier density matching those obtained in longitudinal transistor measurements. This suggests that, even when $\mu < 1\ \mathrm{cm^2\,V^{-1}\,s^{-1}}$, charges in organic semiconductors can still behave as delocalized coherent carriers. This technique paves the way to ubiquitous Hall-effect studies in a wide range of low-mobility materials and devices, where it is typically very difficult to resolve the Hall effect even in very high dc magnetic fields.

DOI: 10.1103/PhysRevApplied.5.034008

I. INTRODUCTION

Charge-carrier transport in organic semiconductors frequently occurs at the borderline between a bandlike coherent motion through extended states and an incoherent hopping via localized states. Intrinsic factors competing for determining the dominant transport mechanism include intermolecular π-π interactions governed by the equilibrium crystal packing (the transfer integrals) [1] and carrier self-localization due to the local electron-phonon coupling in the form of polarons [2–4], as well as nonlocal electron-phonon coupling and off-diagonal thermal disorder [5,6]. In molecular crystals with sufficiently strong intermolecular interactions, bands of delocalized states can form, leading to a bandlike transport, provided that thermal disorder is not too strong (see, e.g., Ref. [7] and references therein). However, because of weak van der Waals interactions, such bands are typically narrow (a few hundred meV), and the carrier mobility μ is intrinsically low ($\mu \sim 0.1$–$20\ \mathrm{cm^2\,V^{-1}\,s^{-1}}$) [1,7] in comparison with inorganic semiconductors, where μ is usually in the range 100–2000 $\mathrm{cm^2\,V^{-1}\,s^{-1}}$ [8]. Thermal disorder can play a dual role: While promoting carrier hopping among molecules in the activated hopping regime, it tends to destroy the extended bands that might exist otherwise and leads to carrier localization and scattering, thus creating localized states below the mobility edge (the tail states) [5,6,9,10]. Such localized tail states do contribute to charge transport by providing a hopping pathway for carriers and participating in multiple trap-and-release processes [7]. It is believed that a crossover between the hopping and bandlike transport regimes occurs in organic field-effect transistors (OFETs) when the charge-carrier mobility is around unity, $\mu \sim 1\ \mathrm{cm^2\,V^{-1}\,s^{-1}}$. Besides these intrinsic factors, static disorder originating from chemical impurities and structural defects also plays a significant role in real-world materials, usually leading to additional trap states in the tail that immobilize charge carriers at various time scales [9,11,12].

The Hall effect represents a powerful tool for the studies of the intrinsic charge-transport properties of organic semiconductors, because the Lorenz force acting on drifting charge carriers in Hall measurements acts on only delocalized (that is, bandlike) charge carriers that have a nonzero microscopic drift velocity, while localized (hopping) carriers are not expected to contribute to Hall voltage by means of a classical Lorenz force (for a review on Hall-effect and transport studies in single-crystal OFETs, see, e.g., Ref. [7] and references therein; for individual Hall-effect studies in various OFETs, see Refs. [13–17]). It would only be fair, however, to mention that a transverse magnetic field effect in a purely hopping transport regime,

---

[*] Present address: Department of Physics, South University of Science and Technology of China, Shenzhen, Guangdong 518055, China.

[†] Corresponding author.
podzorov@physics.rutgers.edu

originating from quantum-interference effects on the hopping probabilities in closed-loop trajectories, has been theoretically predicted [18] but thus far eluded experimental observations [19]. Thus, a classical (band-semiconductor–like) Hall effect observed in an OFET is expected to probe delocalized charge carriers in extended band states and can therefore (a) reveal if such band states exist in the system and (b) give information about the concentration and the intrinsic mobility of charges in these states. Despite the importance of the Hall effect, however, such studies are not widely pursued in organic semiconductors, because it is typically very difficult to resolve Hall voltage in these highly resistive low-μ materials even in high magnetic fields. For example, a Hall voltage presented in an OFET under typical experimental conditions is $V_{\mathrm{Hall}} = WE_{\mathrm{SD}}B\mu$, where $W \sim 0.1$–1 mm is the channel width in a typical Hall bar geometry, $E_{\mathrm{SD}} = 10$–$100\ \mathrm{V\,cm^{-1}}$ is the longitudinal source-drain electric field, B is the magnetic field (typically up to 12 T), and $\mu \sim 1\ \mathrm{cm^2\,V^{-1}\,s^{-1}}$ is the mobility in systems at the borderline between hopping and bandlike transport, thus giving a typical $V_{\mathrm{Hall}} \sim 0.1$–$10$ mV. Electric noise due to carrier hopping and shallow traps can be rather significant and can easily mask the small Hall voltage. Therefore, it is usually very difficult to extract the small Hall signal from a noisy background in OFETs, even if one uses a superconducting magnet and a very high magnetic field of up to 12 T [13–17]. Below, we describe an ac Hall-effect measurement technique that we have developed for OFETs and other low-μ systems. We show that, in comparison with the conventional dc Hall measurements, this method delivers a much more superior signal-to-noise ratio, especially important for Hall-effect studies in low-mobility materials and devices. It is also technically important that high magnetic fields are not necessary in this method. The paper is organized as follows. Section II provides technical details of device fabrication and measurements. Section III describes the charge-transport properties of single-crystal OFETs used in this study and as well provides a description of our ac Hall measurement setup. Section IV describes the basic concept of a phase-sensitive detection of Hall voltage induced by an ac magnetic field and gives the details of our Faraday induction corrected ac Hall-effect measurements. In Sec. V, we discuss the results obtained for two types of OFETs and compare the carrier densities and mobilities measured using the longitudinal OFET transport and the ac Hall effect. Section VI gives the conclusions.

II. METHODS

Rubrene and tetracene single crystals are grown using a physical vapor transport method in a stream of ultrahigh-purity He gas at a sublimation temperature of 320 and 280 °C, respectively (for details, see, e.g., Ref. [7]). For OFET fabrication, electrical contacts are painted on the (***a***, ***b***) facets of the crystals with an aqueous solution of colloidal graphite (Ted Pella) and contacted with 25-μm-thick gold wires. In tetracene OFETs, we use a very thin underlayer of Cytop (<30 nm) topped with a much thicker layer of parylene-*N* (1.35 μm) as a gate insulator (capacitance $C_i = 1.7\ \mathrm{nF\,cm^{-2}}$). Cytop is deposited by spin coating a commercially available Cytop precursor solution at 3000 rpm for 300 s on a flat crystal attached to a solid glass substrate with a thermal wax, followed by a gentle overnight annealing at 60 °C in vacuum, which results in uniform thin films with a thickness of less than 30 nm. Using a Cytop underlayer gives a better signal-to-noise ratio in Hall voltage measurements in tetracene OFETs. In rubrene OFETs, only parylene-*N* gate dielectric (with a typical thickness of 1–1.1 μm) is used ($C_i = 2.1$–$2.3\ \mathrm{nF\,cm^{-2}}$). Gate electrodes are prepared by thermally evaporating silver (35 nm thick) through a shadow mask on top of the parylene-coated crystals. Typical aspect ratios of the channel dimensions in our OFETs are $L/W = 1$–3 and $D/W = 0.4$–1.2, where L is the channel length, W is the channel width, and D is the longitudinal distance between the four-probe voltage probes. All measurements reported in this study are performed at room temperature in air. Keithley Source-Meters K-2400 and Electrometers K-6512 are used for FET measurements. In ac Hall measurements, we use a DL1201 voltage preamplifier (DL Instruments) and a Stanford Research SR-830 lock-in amplifier for Hall voltage measurements, Keithley current source K6221 for I_{SD} excitation, and Electrometer K6514 for four-probe voltage measurements. An ac magnetic field of a frequency 0.5–3 Hz with a root-mean-square magnitude of $B_{\mathrm{rms}} = 0.23$ T is generated by rotating an assembly of strong permanent Nd magnets fixed on an Al frame. The magnet assembly is driven by a dc electromotor (Dayton 3XE22D), which is in turn controlled by a Hewlett-Packard dc power supply HP 6642 A. The rotation speed can be adjusted by varying the output voltage of the power supply. $B(t)$ near the sample is measured in real time by a Bell-5180 Gauss meter, which also generates an output voltage proportional to $B(t)$. We use this voltage as a reference signal for the lock-in. Data acquisition is carried out by interfacing the instruments with a computer through a National Instruments GPIB card controlled by a LabVIEW program.

III. SINGLE-CRYSTAL OFETS AND ac HALL-EFFECT SETUP

Rubrene ($C_{42}H_{28}$) and tetracene ($C_{18}H_{12}$) OFETs used in this study are the top-contact-top-gate devices fabricated on macroscopic vapor-grown single crystals of rubrene and tetracene using graphite paint contacts, low-ε polymers as gate insulators, and evaporated silver gates. For gate dielectrics, we use either 1.1–1.35-μm-thick parylene-*N* films or a combination of extremely thin (<30 nm) Cytop and a thick (approximately 1.35 μm) parylene-*N* (for fabrication details, see Sec. II). For characterization of these OFETs, transconductance characteristics (the channel source-drain current I_{SD} as a function of the gate voltage V_G at a given source-drain voltage V_{SD}) are recorded in the linear and saturation regimes to extract the carrier mobility μ, according to the standard (two-probe) FET equations (see, e.g., Ref. [7]):

$$I_{SD}{}^{\text{lin}} = \frac{W}{L}\mu_{\text{lin}} C_i V_{SD}(V_G - V_T)\ (|V_G| \gg |V_{SD}|),$$
$$I_{SD}{}^{\text{sat}} = \frac{W}{2L}\mu_{\text{sat}} C_i (V_G - V_T)^2\ (|V_G| < |V_{SD}|), \qquad (1)$$

where L and W are the channel's length and width, respectively, C_i is the gate-channel capacitance per unit area ($C_i = 1.7\ \text{nF}\,\text{cm}^{-2}$ in our tetracene OFETs and, depending on the exact thickness of the dielectric, 2.1–2.3 $\text{nF}\,\text{cm}^{-2}$ in our rubrene OFETs), and V_T is a threshold voltage, which is typically small in single-crystal OFETs. Thus, the carrier mobility in the linear and saturation regimes, μ_{lin} and μ_{sat}, respectively, as well as the total carrier density (electrostatically induced above the threshold) n_{FET}, can be found using the following expressions:

$$\mu_{\text{lin}} = \frac{L}{W}\frac{1}{C_i}\frac{1}{V_{SD}}\frac{\partial I_{SD}}{\partial V_G}, \qquad \mu_{\text{sat}} = \frac{2L}{W}\frac{1}{C_i}\left(\frac{\partial\sqrt{|I_{SD}|}}{\partial V_G}\right)^2,$$
$$en_{\text{FET}} = C_i(V_G - V_T). \qquad (2)$$

Figures 1 and 2 show the electric characteristics of the rubrene and tetracene OFETs similar to those used in the present study. Both systems exhibit a standard textbook FET behavior, well described by the above equations, with an extended linear regime in $I_{SD}(V_G)$, in which the mobility is nearly independent of the carrier density and the longitudinal electric field (that is, μ is independent of V_G and V_{SD}, respectively). In the saturation regime, this corresponds to a linear "square-root" transfer curve $|I_{SD}|^{1/2}(V_G)$. The existence of such an extended linear regime is crucial for the correct and reliable extraction of the longitudinal drift field-effect mobility in OFETs. In both types of devices, a good match between the linear and saturation mobilities is observed: $\mu_{\text{sat}} \approx \mu_{\text{lin}}$. The typical mobility at the rubrene/parylene-N interface is around 5–6 $\text{cm}^2\,\text{V}^{-1}\,\text{s}^{-1}$, while the typical mobility at the tetracene/Cytop interface is in the range 0.3–0.8 $\text{cm}^2\,\text{V}^{-1}\,\text{s}^{-1}$. These values are consistent with the dielectric permittivities of parylene-N ($\varepsilon = 2.6$) and Cytop ($\varepsilon = 2$) and with the mobilities obtained in similar single-crystal OFETs in prior studies [7,20–23]. It is worth noting that mobilities obtained in our devices by a gated two-probe technique are similar to the four-probe mobilities, indicating that the contact resistance is relatively small.

In our ac Hall measurements, an ac magnetic field is generated by rotating strong permanent neodymium (Nd) magnets, rigidly assembled on an aluminum frame. The sample is wired inside of a light-proof thin aluminum box, which is placed in the gap between the rotating magnets, so that the magnetic field is perpendicular to the OFET's accumulation channel (a sketch and a photo of the setup are shown in Fig. 3; a video of the setup in operation is available in Ref. [24]). The rotation is driven by a dc electric motor. A Gauss probe placed near the sample is used to measure the magnetic field $B(t)$ and its frequency ω in real time. It generates a small output voltage proportional to $B(t)$, which is supplied back to the lock-in amplifier as a reference. This method of generating an ac B field is more convenient than using electromagnets, in which case specially designed coils and powerful current sources are necessary to achieve magnetic fields greater than 0.2 T. Even if the frequency of magnet rotation slightly fluctuates over time, the lock-in amplifier tracks the actual frequency, which allows the powerful noise discrimination provided by the phase-sensitive detection to be fully utilized without the use of high-precision step motors. In our system, fluctuations of ω are typically slow and are within 2% of its average value. In the case when the generated ac magnetic field $B(t)$ is periodic but not exactly harmonic (that is, does not exactly follow a sine or cosine), the magnetic field amplitude that defines the measured ac Hall voltage is given by the first Fourier harmonic of the $B(t)$ function (at the frequency ω), which can be determined either analytically by taking a Fourier transform of the measured $B(t)$ or experimentally by performing a spectrum analysis using an oscilloscope or a spectrum analyzer. In our setup, this harmonic corresponds to the

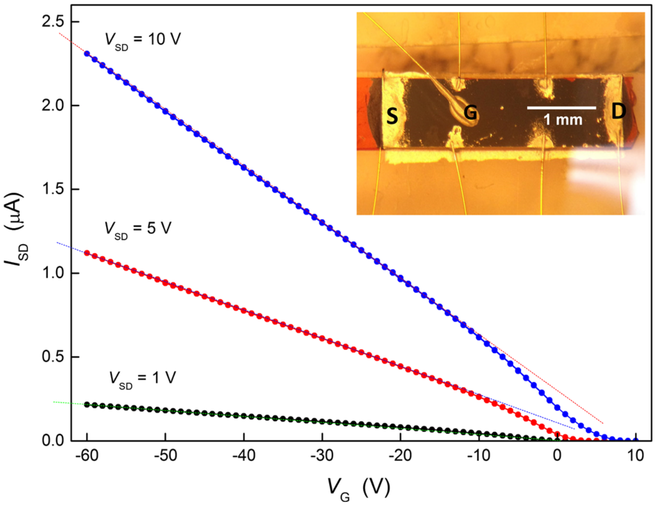

FIG. 1. Transfer characteristics of a single-crystal rubrene OFET. Contacts, graphite paint; gate dielectric, parylene-N; gate electrode, evaporated silver. The inset shows a photo of the device. The two-probe mobility extracted from these characteristics is independent of V_{SD} and V_G. The four-probe mobility (not shown) is comparable to the two-probe mobility: $\mu_{4p} \approx \mu_{2p}$ = 5–6 $\text{cm}^2\,\text{V}^{-1}\,\text{s}^{-1}$. For details on similar devices, see, e.g., Ref. [7] and references therein.

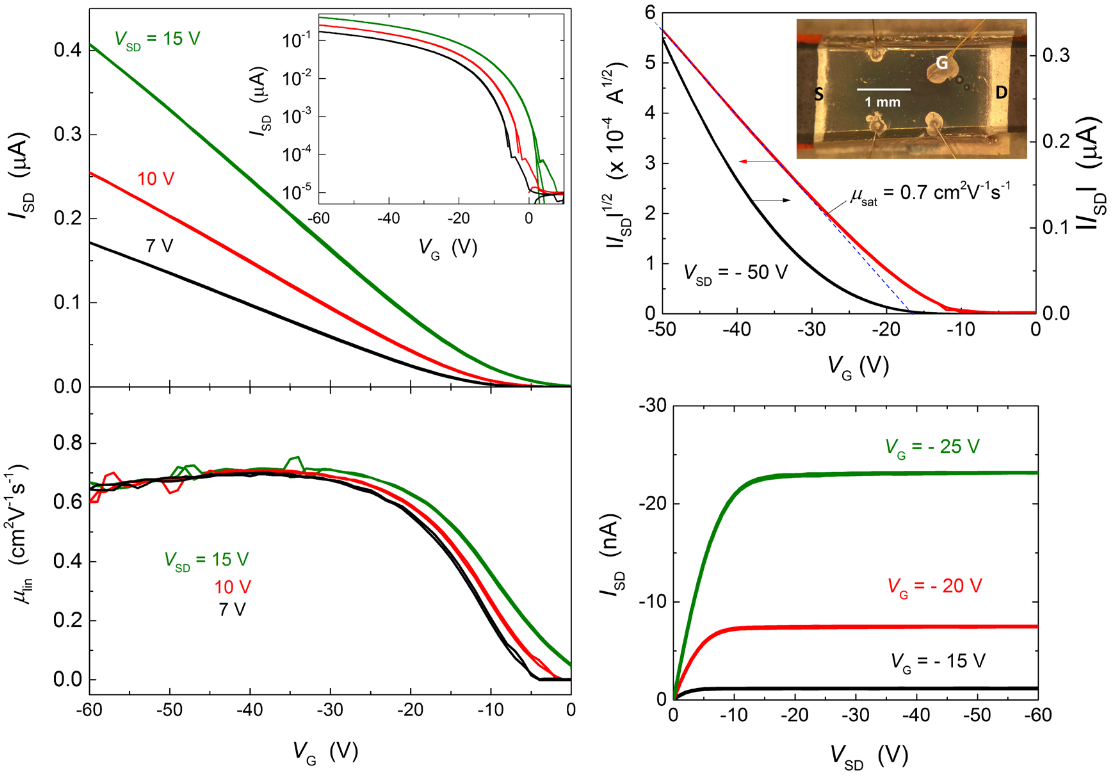

FIG. 2. Characteristics of single-crystal tetracene OFETs. Contacts, graphite paint; gate dielectric, <30-nm-thick Cytop topped with a 1.35-μm-thick parylene-*N*; gate electrode, evaporated silver. The panels show (top to bottom, left to right): linear-regime transfer curves (the inset shows the same data on a semi-log scale), linear mobility vs gate voltage, transfer characteristics in the saturation regime (inset shows the device photo), and the output curves. These characteristics indicate that, although the carrier mobility in tetracene single-crystal OFETs is relatively low (here, $\mu_{\text{lin}} \approx \mu_{\text{sat}} \sim 0.6$–$0.7$ cm^2 V^{-1} s^{-1}), the devices behave as classic textbook FETs.

root-mean-square (rms) magnetic field $B = 0.23$ T. The ac Hall voltage across the channel is measured by a lock-in amplifier tuned to the frequency of the B field tracked by the Gauss meter. The longitudinal dc source-drain voltage, four-probe voltage, and dc source-drain current are applied and measured by Keithley source meters and electrometers.

IV. ac HALL-EFFECT MEASUREMENTS IN OFETS

The phase-sensitive (lock-in) detection technique is widely used to extract small signals from a noisy background, whose fluctuations are often orders of magnitude larger than the signal of interest. In electric measurements, the most common practice is to drive an ac excitation current I through the sample and measure the desired voltage that is phase-locked to the excitation. However, this specific implementation of phase-sensitive detection does not solve the problem of a poor signal-to-noise ratio in conventional Hall-effect measurements. Indeed, with an ac current excitation, the true Hall voltage across the channel, $V_{\text{Hall}} \propto IB$ and the parasitic offset voltage due to unavoidable longitudinal misalignment (or asymmetry) of Hall probes, $V_{\text{offset}} \propto IR_{\text{offset}}(B)$, where $R_{\text{offset}}(B)$ is some effective sample resistance between the misaligned Hall leads, are both modulated at the frequency of the excitation. Therefore, a phase-sensitive detection in this case would not be able to discriminate the true Hall voltage (the signal) from the fluctuating offset (the noisy background). The correct method thus uses an ac magnetic field $B = B_0 \cdot \cos(\omega t)$, applied perpendicular to the channel, while driving a dc longitudinal excitation current through the sample (Fig. 3). In that case, V_{Hall} is modulated at the frequency of the B field, whereas V_{offset} shows either no modulation (if there is no magnetoresistance) or changes at higher harmonics (2ω, 4ω, 6ω, etc.), because the magnetoresistance of most materials is an even function of B and thus does not lead to a signal at the first harmonic. Phase-sensitive detection can then be used to selectively measure the true Hall voltage.

In general, the total voltage across the Hall probes, V_H, is composed not only of the true ac Hall voltage V_{Hall} but also an ac Faraday induction electromotive force V_F, because the electric circuit connected to the Hall probes forms a closed loop, through which an ac magnetic field passes. The magnitude of the Faraday induction depends on both the frequency of the magnetic field and the effective area S of the loop: $V_F \propto -SdB/dt = SB_0\omega \sin(\omega t)$. This parasitic signal can be minimized by carefully wiring the sample in such a way that the area of the loop S is as small

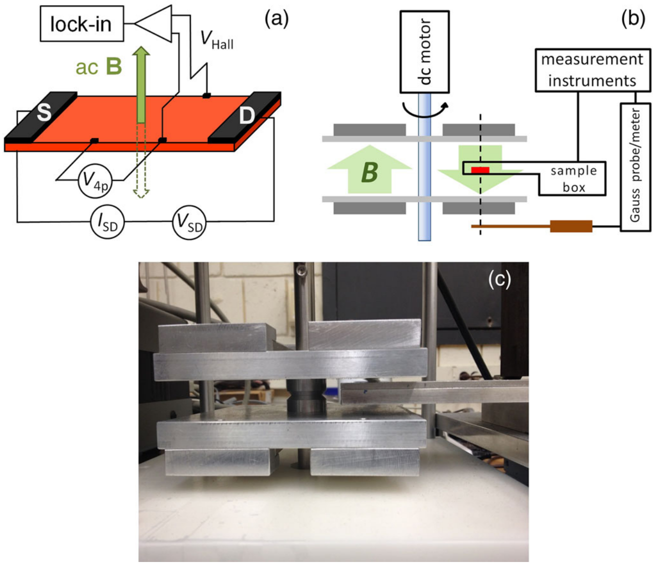

FIG. 3. (a) A diagram of ac Hall-effect measurements utilizing an ac magnetic field, a dc source-drain current excitation, and a phase-sensitive detection of Hall voltage (the gate electrode is omitted for clarity). (b) Schematic side view of the measurement setup, showing the rotating frame with Nd magnets that create a vertical ac magnetic field, a sample (red) in the sample box, and a Gauss meter connected to the instruments. (c) A photograph of the flat sample box inserted between the magnets. A video showing the entire setup in operation can be viewed in Ref. [24].

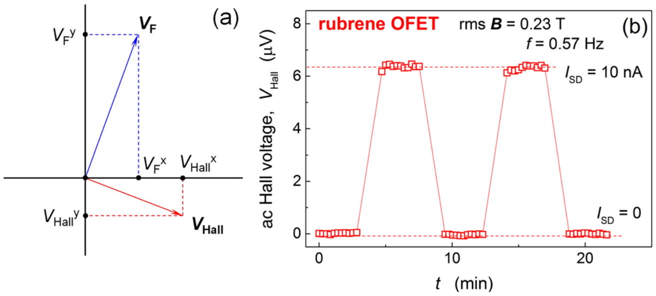

FIG. 4. (a) Vector representation of the Faraday induction electromotive force $\mathbf{V_F}$ and the true Hall voltage $\mathbf{V_{Hall}}$ presented across the Hall voltage leads in ac Hall-effect measurements. The horizontal and vertical axes correspond to the signals phase shifted by 0 and $\pi/2$, respectively, relatively to the reference signal supplied to the lock-in amplifier. The values measured in the experiment on the lock-in's X and Y channels are the x and y components of the total rms voltage detected between the Hall voltage leads, $\mathbf{V_H} = \mathbf{V_{Hall}} + \mathbf{V_F}$. When a dc longitudinal current is flown through the sample ($I_{SD} \neq 0$), both $\mathbf{V_F}$ and $\mathbf{V_{Hall}}$ are generated by the ac magnetic field, while for zero-current excitation ($I_{SD} = 0$), only $\mathbf{V_F}$ is present. Thus, the true Hall voltage $|\mathbf{V_{Hall}}| \equiv [(V_{Hall}{}^x)^2 + (V_{Hall}{}^y)^2]^{1/2}$ can be found as $|\mathbf{V_{Hall}}| \equiv [(V_I^x - V_0^x)^2 + (V_I^y - V_0^y)^2]^{1/2}$, where $\mathbf{V_I}$ and $\mathbf{V_0}$ are the total voltages measured between the Hall leads at $I_{SD} \neq 0$ and $I_{SD} = 0$, respectively [Eq. (3)]. (b) The rms value of ac Hall voltage measured in a single-crystal rubrene OFET in a very small ac magnetic field, rms $B = 0.23$ T ($f = 0.57$ Hz) at $V_G = -20$ V. The two stages of the measurement, on and off, corresponding to $I_{SD} = 0$ (set by $V_{SD} = 0$) and $I_{SD} = 10$ nA (set by $V_{SD} = 0.1$ V), are shown. Even though the Hall voltage is extremely small (approximately 6 μV), the signal resolution is excellent (Hall voltage fluctuations are less than 0.3 μV). The Hall mobility and carrier density extracted from these data, $\mu_{Hall} = 5.8 \pm 0.05\,\mathrm{cm^2\,V^{-1}\,s^{-1}}$ and $n_{Hall} = (2.26 \pm 0.02) \times 10^{11}\,\mathrm{cm^{-2}}$, respectively, agree well with those obtained in four-probe longitudinal FET measurements.

as possible and by performing measurements at a low frequency. In addition, most organic samples have a rather high resistivity, which gives another reason for working at low frequencies: Parasitic capacitance distributed over the measurement circuit may shunt sample impedance at high frequencies. Usually, $f = \omega/2\pi \sim 0.5$–2.5 Hz should be used for most OFETs. Nevertheless, even when working at a low frequency with a carefully minimized wiring loop, the Faraday induction may still be comparable to or even greater than the true Hall signal, especially in low-mobility samples with $\mu < 1\ \mathrm{cm^2\,V^{-1}\,s^{-1}}$. Fortunately, the Faraday induction signal is rather stable, since the fluctuations in ω are typically less than 2%, and the loop area enclosed by the wires is constant for a given measurement. Therefore, V_F can be measured as a stable background at zero excitation current (that is, at $V_{SD} = I_{SD} = 0$, yet with the gate voltage applied, which in p-type OFETs corresponds to $V_G < 0$). At these conditions, the true Hall voltage is zero: $V_{Hall} = 0$. V_F can then be subtracted from the total signal V_H measured at a finite excitation (V_{SD}, $I_{SD} > 0$) and at the same $V_G < 0$. In addition, we note that, according to its definition, the Faraday induction is phase shifted with respect to B and the true V_{Hall} by $\pi/2$, which provides an additional way of discriminating it from the true Hall voltage [Fig. 4(a)].

Phase-sensitive detection measures both the rms magnitude and the phase angle of the total voltage presented across the Hall voltage leads, V_H, with respect to the reference signal proportional to $B(t)$. Alternatively, it measures V_H's x and y components $V_H{}^x$ and $V_H{}^y$, respectively (note that x and y superscripts here do not refer to the real-space coordinates but rather correspond to the two signals detected on the lock-in's X and Y channels, with the x channel being in phase with the reference signal and y channel being phase shifted by $\pi/2$). In our setup, in the ideal situation of a negligible parasitic capacitance, the true Hall voltage has a phase angle of zero (only x component), and the Faraday induction has a phase angle of 90° (only y component). This is because the Hall voltage is proportional to B, whereas the Faraday induction is proportional to dB/dt. In reality, however, phase angles of both the true Hall voltage and the Faraday induction show some small deviation from the above ideal values, which is schematically depicted at Fig. 4(a), and, thus, $V_H{}^x = V_{Hall}{}^x + V_F{}^x$ and $V_H{}^y = V_{Hall}{}^y + V_F{}^y$. Therefore, the proper way of extracting the rms value of the pure Hall voltage V_{Hall} is to perform a vector subtraction of the background signal measured at $I_{\mathrm{SD}} = 0$ (the Faraday induction only, $\mathbf{V_F}$) from the total signal measured at $I_{\mathrm{SD}} > 0$ ($\boldsymbol{V}_{\mathbf{H}} = \boldsymbol{V}_{\mathbf{Hall}} + \boldsymbol{V}_{\mathbf{F}}$):

$$|\mathbf{V_{Hall}}| \equiv \sqrt{(V^x_{\mathrm{Hall}})^2 + (V^y_{\mathrm{Hall}})^2} = \sqrt{(V^x_I - V^x_0)^2 + (V^y_I - V^y_0)^2}, \qquad (3)$$

where $\boldsymbol{V}_{\mathbf{I}}$ and $\boldsymbol{V}_{\mathbf{0}}$ are the total voltages measured between the Hall leads at $I_{\mathrm{SD}} \neq 0$ and $I_{\mathrm{SD}} = 0$, respectively. Thus, we perform cycles of measurements, each composed of a zero-current stage followed by a finite-current stage, with several cycles usually taken to average the obtained true V_{Hall} signal [Fig. 4(b)]. A dedicated LabVIEW program records the x and y lock-in signals in the *off* and *on* stages, performs a vector subtraction according to Eq. (3), and extracts the correct Hall carrier density and mobility according to the formulas

$$n_{\mathrm{Hall}} = \frac{I_{\mathrm{SD}}B}{eV_{\mathrm{Hall}}} = \frac{\sigma_{4p}B}{e}\frac{W}{D}\frac{V_{4p}}{V_{\mathrm{Hall}}},$$
$$\mu_{\mathrm{Hall}} \equiv \frac{\sigma_{4p}}{en_{\mathrm{Hall}}} = \frac{1}{B}\frac{D}{W}\frac{V_{\mathrm{Hall}}}{V_{4p}}, \qquad (4)$$

where the ac variables B and V_{Hall} are taken in their rms form [that is, here, $B = 0.23$ T and V_{Hall} defined by Eq. (3)], σ_{4p} is the four-probe channel conductivity per square, D is the distance between the voltage probes in the four-probe configuration, and V_{4p} is the four-probe voltage (other parameters are defined above).

Figure 4(b) shows an example of ac Hall voltage recorded in two stages, $I_{\mathrm{SD}} = 0$ and 10 nA, in a pristine single-crystal rubrene OFET with a parylene gate insulator, performed at $V_G = -20$ V, $V_{\mathrm{SD}} = 0.1$ V, and $B_{\mathrm{rms}} = 0.23$ T ($f = 0.57$ Hz). Here, we use crystalline rubrene as our test material, because since their discovery in 2003 [21,22], rubrene OFETs represent benchmark high-performance organic transistors, well characterized in various device configurations [7,13,14,16,25]. In this measurement, an extremely small Hall voltage of 6.35 μV is easily resolved. We note that the observed Hall voltage is more than 3 orders of magnitude smaller than V_{Hall} estimated above for conventional Hall measurements in a high dc magnetic field of 10 T, which makes sense, because the other parameters in our experiment (B and I_{SD}) are extremely small. Yet, it results in the correct Hall carrier density and mobility, comparable to those obtained in rubrene OFETs by the conventional Hall-effect technique [13,14]. The important distinction here is that the signal-to-noise ratio in our ac Hall method is much superior to that in the conventional dc Hall measurements. The mobility and carrier density extracted from the data in Fig. 4(b) are $\mu_{\mathrm{Hall}} = 5.8 \pm 0.05$ cm^2 V^{-1} s^{-1} and $n_{\mathrm{Hall}} = (2.26 \pm 0.02) \times 10^{11}$ cm^{-2}, respectively, which agree well with the results obtained in longitudinal four-probe OFET measurements of the same device. This demonstration shows the remarkable resolving power of the ac Hall-effect technique described here.

Although the above procedure allows us to largely get rid of the Faraday induction artifacts in ac Hall measurements, we find that an additional measurement, a frequency dependence, is necessary in certain cases of low-mobility OFETs or OFETs with a significant contact resistance. Indeed, the vector subtraction procedure described earlier assumes that the Faraday induction signal is the same (phase- and amplitudewise) in the *on* and *off* stages of the measurement. This should indeed be the case in “ideal” or “well-behaved” FETs, as long as the same gate voltage is applied during both stages. Such a situation is realized, for instance, in rubrene single-crystal OFETs, where an efficient carrier injection from contacts occurs even at zero source-drain bias ($V_{\mathrm{SD}} = I_{\mathrm{SD}} = 0$), and an accumulation channel is formed, as long as $V_G < 0$ is applied [7,22]. In such a case, the portion of the accumulation channel between the Hall voltage probes that “connects” them together, thus forming a closed loop, has the same density of charge carriers, resistivity, capacitance, and inductance at both the *on* and *off* stages. However, this may not be the case in OFETs with large Schottky contact barriers, where a significant source-drain voltage must be applied, in addition to V_G, to inject carriers and form an accumulation channel. Besides, in the systems dominated by shallow traps or tail states, carrier mobility may steeply depend on the longitudinal electric field, which can make the channel conductivity be different at the *on* and *off* stages [26]. In such cases, we find that the apparent ac Hall voltage exhibits a linear dependence on frequency, signaling that not all of the Faraday induction has been removed by the data analysis discussed earlier. The linear dependence, however, allows us to unambiguously determine the true Hall mobility by extrapolating ${\mu_{\mathrm{Hall}}}^{\mathrm{ac}}(f)$ dependence to $f = 0$ (zero-frequency limit), at which the Faraday induction contribution is zero. This zero-frequency offset corresponds to the true Hall mobility μ_0. Therefore, the correct ac Hall measurements in OFETs should include a frequency-dependent measurement to find a zero-frequency offset.

Examples of such f-dependent measurements are shown in Fig. 5 for pristine rubrene and tetracene single-crystal OFETs. The rubrene OFET does not exhibit any frequency dependence, with the true Hall mobility $\mu_0 = 5.1$ cm^2 V^{-1} s^{-1} [Fig. 5(a)], while the tetracene OFET does show a frequency dependence with a finite zero-frequency offset corresponding to the true Hall mobility of $\mu_0 = 0.3$ cm^2 V^{-1} s^{-1} [Fig. 5(b)]. It is worth noting that, in tetracene OFETs, measurements at an increasing V_{SD} result in a weaker frequency dependence, which is consistent with the notion of a suppressed contact resistance at a higher

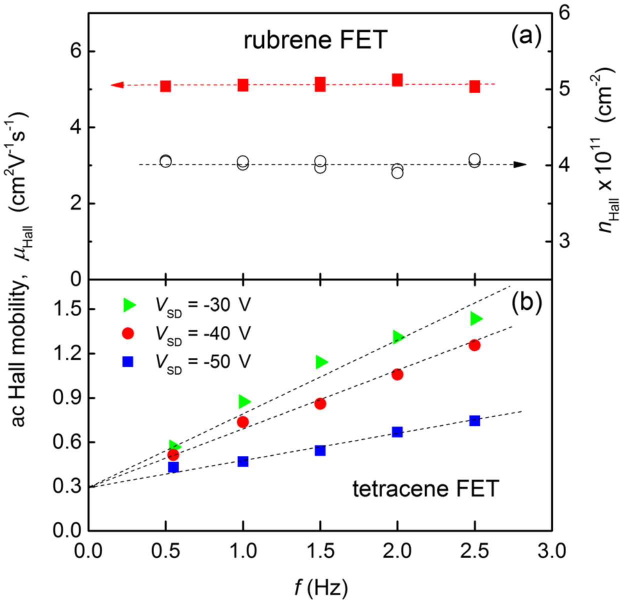

FIG. 5. Dependence of the apparent ac Hall mobility on the frequency of an ac B field in two representative systems, with the intrinsic Hall mobility μ_0 identified as the zero-frequency offset: (a) single-crystal rubrene OFETs, where μ_{Hall} and n_{Hall}, measured at rms $B = 0.23$ T, $V_G = -30$ V, and $I_{\mathrm{SD}} = 100$ nA (set by $V_{\mathrm{SD}} = 1$ V), are found to be frequency independent, yielding the intrinsic Hall mobility $\mu_0 = 5.1$ cm^2 V^{-1} s^{-1}; (b) single-crystal tetracene OFETs, where the linear fits to the frequency dependence obtained at three different V_{SD} converge at the same zero-frequency limit, yielding the intrinsic Hall mobility $\mu_0 = 0.3$ cm^2 V^{-1} s^{-1}.

source-drain voltage in OFETs [22]. We note that transistors that do not have delocalized charge carriers (such as in a purely hopping regime) are not expected to exhibit a classical Hall effect. Although a nonzero (apparent) ac Hall voltage at finite frequencies is expected in such devices due to the small residual Faraday induction, taking a zero-frequency limit should result in $V_{\mathrm{Hall}} = 0$ and $\mu_0 = 0$ (a straight line passing through the origin). Thus, performing the frequency dependence check in ac Hall-effect studies is important. In all further discussions of the ac Hall measurements below, we use either zero-frequency offsets or values obtained at the lowest frequency of 0.5 Hz, at which the error is negligible.

V. COMPARISON OF FET AND ac HALL-EFFECT MEASUREMENTS

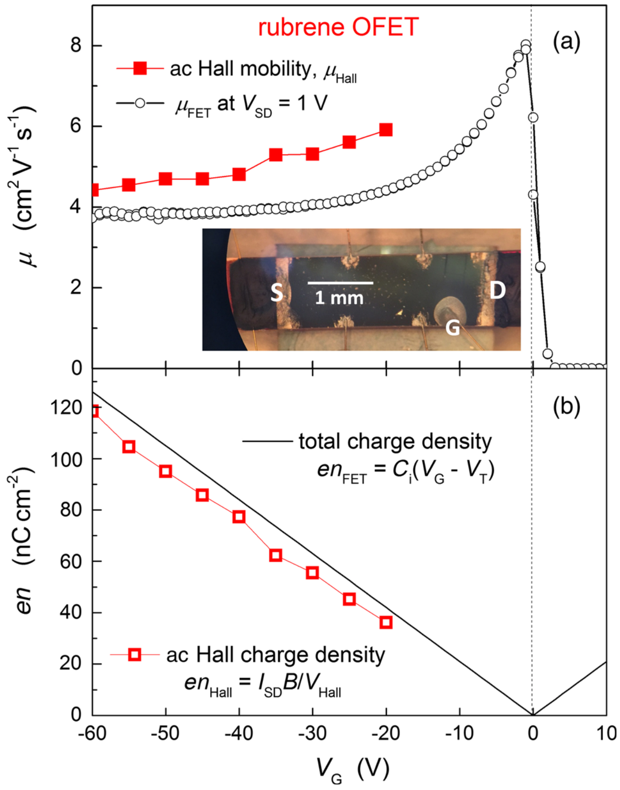

FIG. 6. The ac Hall-effect ($B_{\mathrm{rms}} = 0.23$ T) and conventional FET measurements in single-crystal rubrene OFETs. (a) A linear-regime FET mobility (open circles) is compared with the mobility obtained in ac Hall measurements (solid squares). (b) The total electrostatic carrier density (solid line) is compared with the carrier density extracted from ac Hall measurements using Eq. (4) (open squares). A good match between Hall-effect and FET carrier mobilities and densities is observed, as expected for a coherent transport of delocalized carriers and consistent with the prior observations in dc Hall-effect studies of rubrene OFETs.

Figures 6 and 7 present a comparison between the ac Hall-effect and FET measurements of rubrene and tetracene single-crystal OFETs. As described in Sec. III, both rubrene and tetracene OFETs studied here exhibit a textbook FET behavior with an extended linear regime in $I_{\mathrm{SD}}(V_G)$ characteristics, signifying a mobility nearly independent of the carrier density [seen as the plateaus in Figs. 6(a) and 7(a)]. We emphasize that such a linear regime is crucial for an unambiguous extraction of the longitudinal field-effect drift mobility [for other criteria of applicability of the standard FET equations (1) and (2), see, e.g., Ref. [7]]. The drift mobility extracted from the saturation regime measurements matches well that obtained in the linear regime, $\mu_{\mathrm{sat}} \approx \mu_{\mathrm{lin}}$. For details of these transistor measurements, see Sec. III.

ac Hall-effect measurements in these representative single-crystal OFETs yield Hall mobilities and carrier densities matching those obtained from the conventional longitudinal FET measurements (Figs. 6 and 7), thus suggesting that the Hall effect in these OFETs is fully developed. It is worth noting that an underdeveloped Hall effect, characterized with $\mu_{\mathrm{Hall}} < \mu_{\mathrm{FET}}$ and $n_{\mathrm{Hall}} \equiv (I_{\mathrm{SD}}B)(eV_{\mathrm{Hall}})^{-1} > n_{\mathrm{FET}} \equiv e^{-1}C_i(V_G - V_T)$, is reported for several organic semiconductors, including pentacene [27]. These observations have prompted an empirical conclusion that an underdeveloped Hall effect typically occurs in systems where off-diagonal thermal disorder is sufficiently strong to lead to a *partial* carrier coherence.

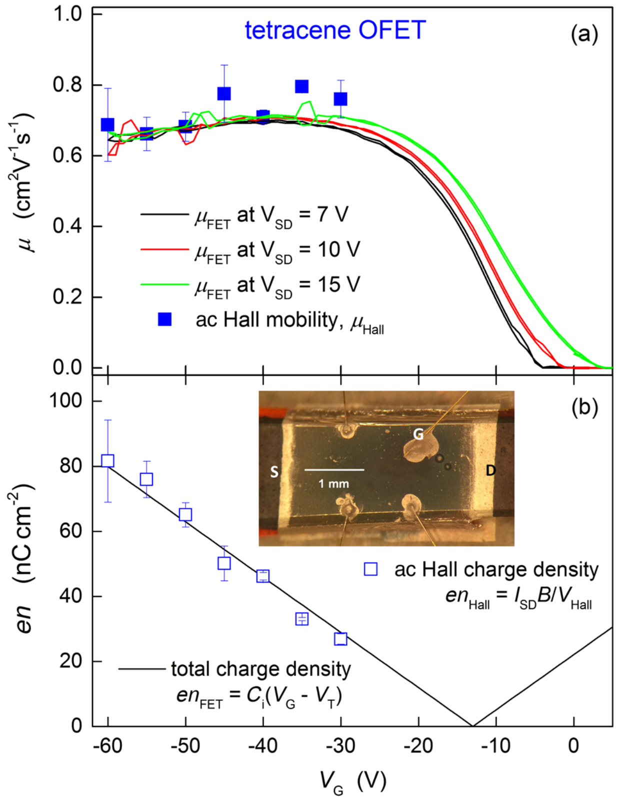

FIG. 7. The ac Hall-effect ($B_{\rm rms} = 0.23$ T) and conventional FET measurements in single-crystal tetracene OFETs. (a) A linear-regime FET mobility measured at three different $V_{\rm SD}$ values (solid lines) is compared with the mobility extracted from ac Hall measurements (solid squares). (b) The total electrostatic carrier density (solid line) and the carrier density extracted from ac Hall measurements using Eq. (4) (open squares) as a function of V_G. Contrary to the common expectation, this low-μ system exhibits a Hall effect with a good match between the Hall and FET carrier densities and mobilities, indicating that, even when mobility is below 1 cm^2 V^{-1} s^{-1}, charge carriers in organic semiconductors can be coherent.

The carrier coherence can be parametrized by a coherence factor α, defined as the ratio of the total carrier density above the threshold, $n_{\rm FET}$, to the carrier density extracted from the Hall effect measurements, $n_{\rm Hall}$. In systems with an underdeveloped Hall effect, the carrier coherence factor is thus $\alpha < 1$, while in systems with a fully developed Hall effect, $\alpha \approx 1$ [7,27,28]. The microscopic details of partial carrier coherence require further investigation, although it is believed that organic semiconductors at the borderline between band and hopping transport, characterized with a low carrier mobility of $\mu \sim 1$ cm^2 V^{-1} s^{-1}, would be more prone to exhibiting an underdeveloped Hall effect ($\alpha < 1$), compared to the systems with a high charge-carrier mobility of $\mu \sim 5$–20 cm^2 V^{-1} s^{-1}. Indeed, in several cases of high-mobility organic semiconductors, the Hall effect is reported to be fully developed, $\mu_{\rm Hall} \approx \mu_{\rm FET}$ and $n_{\rm Hall} \approx n_{\rm FET}$ ($\alpha \approx 1$) (see, e.g., Refs. [7,28]). The surprising observation in this work is that a system with a very low carrier mobility of approximately 0.3 cm^2 V^{-1} s^{-1} (tetracene OFETs) not only shows a Hall effect but also exhibits a fully developed Hall effect with matching Hall and FET mobilities and carrier densities. This suggests that (a) even with such a low mobility, carrier delocalization in organic semiconductors is possible and (b) the Hall effect in this system may not be well described by the model based on partial carrier coherence alone. Indeed, this model predicts that systems with carrier mobilities smaller than that in pentacene should exhibit an even more underdeveloped Hall effect with $\alpha < 1$ [29]. Therefore, our observation signals the need for further experimental and theoretical work aimed at a comprehensive understanding of charge-carrier transport and the Hall effect in organic semiconductors. This effort, however, is beyond the scope of this paper, which has its sole goal of reporting a highly sensitive ac Hall-effect measurement technique for the extraction of intrinsic charge-transport parameters in a wide range of low-mobility systems.

VI. CONCLUSIONS

In conclusion, we develop a powerful ac Hall-effect measurement technique that can be used for high-precision measurements of intrinsic carrier mobility and carrier density, carried out in very low magnetic fields (smaller than 0.25 T) and capable of resolving the Hall effect in OFETs with carrier mobilities as low as 0.3 cm^2 V^{-1} s^{-1}. The method is applicable to a variety of semiconductor devices but is particularly indispensable for investigation of the intrinsic charge transport in low-mobility systems.

ACKNOWLEDGMENTS

We thank Michael Gershenson for helpful discussions and Hyun Ho Choi for assistance with device fabrication. We are indebted to the Institute for Advanced Materials and Devices for Nanotechnology (IAMDN) and the Department of Physics of Rutgers University for providing the necessary facilities and resources to support this project. This work has been carried out in its entirety at the Department of Physics of Rutgers University, New Jersey, USA. We acknowledge the financial support of this work by the National Science Foundation Grant No. DMR-1506609.

[1] D. A. da Silva Filho, E.-G. Kim, and J.-L. Bredas, Transport properties in the rubrene crystal: Electronic coupling and vibrational reorganization energy, Adv. Mater. **17**, 1072 (2005).

[2] J. L. Bredas, D. Beljonne, V. Coropceanu, and J. Cornil, Charge-transfer and energy-transfer processes in pi-conjugated oligomers and polymers: A molecular picture, Chem. Rev. **104**, 4971 (2004).

[3] V. Coropceanu, J. Cornil, D. A. da Silva, Y. Olivier, R. Silbey, and J. L. Bredas, Charge transport in organic semiconductors, Chem. Rev. **107**, 926 (2007).

[4] K. Hannewald and P. A. Bobbert, *Ab initio* theory of charge-carrier conduction in ultrapure organic crystals, Appl. Phys. Lett. **85**, 1535 (2004).

[5] A. Troisi and G. Orlandi, Charge-Transport Regime of Crystalline Organic Semiconductors: Diffusion Limited by Thermal Off-Diagonal Electronic Disorder, Phys. Rev. Lett. **96**, 086601 (2006).

[6] D. L. Cheung and A. Troisi, Modelling charge transport in organic semiconductors: From quantum dynamics to soft matter, Phys. Chem. Chem. Phys. **10**, 5941 (2008).

[7] V. Podzorov, Organic single crystals: Addressing the fundamentals of organic electronics, MRS Bull. **38**, 15 (2013).

[8] S. M. Sze, *Physics of Semiconductor Devices* (Wiley, New York, 1981).

[9] S. Ciuchi and S. Fratini, Electronic transport and quantum localization effects in organic semiconductors, Phys. Rev. B **86**, 245201 (2012).

[10] R. S. Sánchez-Carrera, P. Paramonov, G. M. Day, V. Coropceanu, and J.-L. Brédas, Interaction of charge carriers with lattice vibrations in oligoacene crystals from naphthalene to pentacene, J. Am. Chem. Soc. **132**, 14437 (2010).

[11] C. Krellner, S. Haas, C. Goldmann, K. P. Pernstich, D. J. Gundlach, and B. Batlogg, Density of bulk trap states in organic semiconductor crystals: Discrete levels induced by oxygen in rubrene, Phys. Rev. B **75**, 245115 (2007).

[12] R. Noriega, J. Rivnay, K. Vandewal, F. P. V. Koch, N. Stingelin, P. Smith, M. F. Toney, and A. Salleo, A general relationship between disorder, aggregation and charge transport in conjugated polymers, Nat. Mater. **12**, 1038 (2013).

[13] V. Podzorov, E. Menard, J. A. Rogers, and M. E. Gershenson, Hall Effect in the Accumulation Layers on the Surface of Organic Semiconductors, Phys. Rev. Lett. **95**, 226601 (2005).

[14] J. Takeya, K. Tsukagoshi, Y. Aoyagi, T. Takenobu, and Y. Iwasa, Hall effect of quasi-hole gas in organic single-crystal transistors, Jpn. J. Appl. Phys. **44**, L1393 (2005).

[15] S. Wang, M. Ha, M. Manno, C. D. Frisbie, and C. Leighton, Hopping transport and the Hall effect near the insulator–metal transition in electrochemically gated poly(3-hexylthiophene) transistors, Nat. Commun. **3**, 1210 (2012).

[16] W. Xie, S. Wang, X. Zhang, C. Leighton, and C. D. Frisbie, High Conductance 2D Transport around the Hall Mobility Peak in Electrolyte-Gated Rubrene Crystals, Phys. Rev. Lett. **113**, 246602 (2014).

[17] N. A. Minder, S. Ono, Z. Chen, A. Facchetti, and A. F. Morpurgo, Band-like electron transport in organic transistors and implication of the molecular structure for performance optimization, Adv. Mater. **24**, 503 (2012).

[18] T. Holstein, Hall Effect in Impurity Conduction, Phys. Rev. **124**, 1329 (1961).

[19] R. S. Klein, Investigation of the Hall effect in impurity-hopping conduction, Phys. Rev. B **31**, 2014 (1985).

[20] R. W. I. de Boer, M. E. Gershenson, A. F. Morpurgo, and V. Podzorov, Organic single-crystal field-effect transistors, Phys. Status Solidi **201**, 1302 (2004).

[21] V. Podzorov, V. M. Pudalov, and M. E. Gershenson, Field-effect transistors on rubrene single crystals with parylene gate insulator, Appl. Phys. Lett. **82**, 1739 (2003).

[22] V. Podzorov, S. E. Sysoev, E. Loginova, V. M. Pudalov, and M. E. Gershenson, Single-crystal organic field effect transistors with the hole mobility ~8 cm2/Vs, Appl. Phys. Lett. **83**, 3504 (2003).

[23] Y. Xia, V. Kalihari, C. D. Frisbie, N. K. Oh, and J. A. Rogers, Tetracene air-gap single-crystal field-effect transistors, Appl. Phys. Lett. **90**, 162106 (2007).

[24] A video of the ac Hall-effect measurement setup in operation can be viewed at http://www.physics.rutgers.edu/~podzorov/.

[25] B. Blülle, R. Häusermann, and B. Batlogg, Approaching the Trap-Free Limit in Organic Single-Crystal Field-Effect Transistors, Phys. Rev. Applied **1**, 034006 (2014).

[26] C. R. Newman, R. J. Chesterfield, J. A. Merlo, and C. D. Frisbie, Transport properties of single-crystal tetracene field-effect transistors with silicon dioxide gate dielectric, Appl. Phys. Lett. **85**, 422 (2004).

[27] T. Uemura, M. Yamagishi, J. Soeda, Y. Takatsuki, Y. Okada, Y. Nakazawa, and J. Takeya, Temperature dependence of the Hall effect in pentacene field-effect transistors: Possibility of charge decoherence induced by molecular fluctuations, Phys. Rev. B **85**, 035313 (2012).

[28] J. Takeya, *Chemical Science of π-Electron Systems* (Springer, New York, 2015), pp. 589–604.

[29] T. Fukami, H. Ishii, N. Kobayashi, T. Uemura, K. Sakai, Y. Okada, J. Takeya, and K. Hirose, Correlation between thermal fluctuation effects and phase coherence factor in carrier transport of single-crystal organic semiconductors, Appl. Phys. Lett. **106**, 143302 (2015).